



UNIVERSITY OF LEEDS

This is a repository copy of *Spectral Filtering as a Tool for Two-Dimensional Spectroscopy: A Theoretical Model*.

White Rose Research Online URL for this paper:  
<http://eprints.whiterose.ac.uk/133173/>

Version: Supplemental Material

---

**Article:**

Green, D, Camargo, FVA, Heisler, IA et al. (2 more authors) (2018) Spectral Filtering as a Tool for Two-Dimensional Spectroscopy: A Theoretical Model. *Journal of Physical Chemistry A*, 122 (30). pp. 6206-6213. ISSN 1089-5639

<https://doi.org/10.1021/acs.jpca.8b03339>

---

© 2018 American Chemical Society. This is an author produced version of a paper published in *Journal of Physical Chemistry A*. Uploaded in accordance with the publisher's self-archiving policy.

**Reuse**

Items deposited in White Rose Research Online are protected by copyright, with all rights reserved unless indicated otherwise. They may be downloaded and/or printed for private study, or other acts as permitted by national copyright laws. The publisher or other rights holders may allow further reproduction and re-use of the full text version. This is indicated by the licence information on the White Rose Research Online record for the item.

**Takedown**

If you consider content in White Rose Research Online to be in breach of UK law, please notify us by emailing [eprints@whiterose.ac.uk](mailto:eprints@whiterose.ac.uk) including the URL of the record and the reason for the withdrawal request.



[eprints@whiterose.ac.uk](mailto:eprints@whiterose.ac.uk)  
<https://eprints.whiterose.ac.uk/>

# Spectral Filtering as a Tool for Two-Dimensional Spectroscopy: A Theoretical Model

## SUPPORT INFORMATION

Dale Green,<sup>†</sup> Franco V. A. Camargo,<sup>†,¶</sup> Ismael A. Heisler,<sup>†</sup> Arend G. Dijkstra,<sup>‡</sup>  
and Garth A. Jones<sup>\*,†</sup>

<sup>†</sup>*School of Chemistry, University of East Anglia, Norwich Research Park, Norwich, NR4  
7TJ, UK*

<sup>‡</sup>*School of Chemistry, University of Leeds, Leeds, LS2 9JT, UK*

<sup>¶</sup>*CAPES Foundation, Ministry of Education of Brazil, Brasilia DF 70040-202, Brazil*

E-mail: garth.jones@uea.ac.uk

This document contains a complete description of the theoretical model used in this study, in support of the summary presented in the main text. All Liouville pathways involved in the analysis are presented, as well as further details of the porphyrin monomer modelled and additional examples of the calculated 2D spectra.

## Porphyrin Monomer

In this work we model the same bisalkynyl porphyrin molecule used by Camargo et al in reference 1, for which the linear absorption spectrum shows three bands, associated with three accessible excited singlet states. The lowest in energy of these,  $S_1$ , corresponds to the  $Q$  band, which has a maximum for the fundamental transition at  $15\,650\text{ cm}^{-1}$ . The second band,  $B$ , (ca.  $21\,000 - 24\,000\text{ cm}^{-1}$ ) to  $S_2$  is significantly more intense than the  $Q$  band and the third band,  $N$  to  $S_3$  is very weak, but very broad (ca.  $28\,000 - 34\,000\text{ cm}^{-1}$ ). Asymmetric substituents on the porphyrin macrocycle result in a lowering of the molecule's symmetry from  $D_{4h}$  to  $D_{2h}$ , separating the dipole moment into individual  $x$  and  $y$  contributions. The  $Q_x$  band shows a clear vibronic progression due to coupling to a zinc-porphyrin breathing mode of  $375\text{ cm}^{-1}$ . The shallow band at ca.  $17\,000\text{ cm}^{-1}$  contains contributions from  $Q_y$  as well as  $Q_x$  overtones resulting from coupling to a higher energy vibrational mode of  $1340\text{ cm}^{-1}$ .<sup>2-4</sup>

The structure of the bisalkynyl zinc porphyrin and its linear absorption spectrum are presented in figure S1, reproduced from reference 1. Here we restrict our model to the vibronic  $Q_x$  band and consider coupling to only the  $375\text{ cm}^{-1}$  mode. We assume any contribution from  $Q_y$  is small because the maximum  $Q_y$  intensity is less than 30% of the maximum  $Q_x$  intensity, causing the vibronic progressions associated with  $Q_y$  to be similarly weaker, and  $Q_y$  to  $Q_x$  relaxation takes place in 110 fs or less.<sup>5</sup> Accounting for energy transfer between modes is beyond the scope of this work, where the inclusion of additional modes rapidly increases the size of the system Hilbert space, significantly increasing computation time.

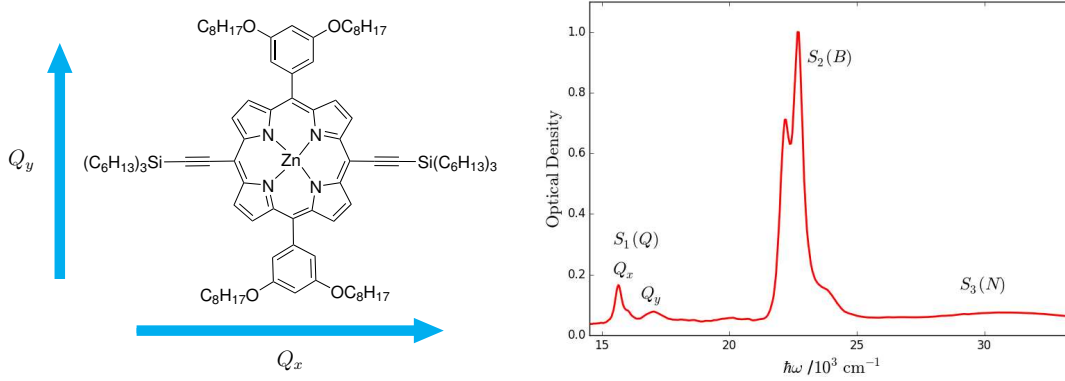


Figure S1: Molecular structure (left) and linear absorption spectrum (right) of the 5,15-bisalkynyl zinc porphyrin monomer.

## Theoretical Model

### Vibronic Hamiltonian

The system Hamiltonian is constructed from the ground,  $|g\rangle$ , and first excited,  $|e\rangle$ , electronic states,

$$H_S = |g\rangle h_g \langle g| + |e\rangle h_e \langle e| \quad (S1)$$

where intramolecular vibrational modes are introduced in the nuclear Hamiltonians as the sum of simple harmonic oscillators,<sup>6</sup>

$$h_g = \sum_j \left[ \frac{p_j^2}{2m_j} + \frac{1}{2} m_j \omega_j^2 q_j^2 \right] \quad (S2)$$

$$h_e = \hbar\omega_{eg}^0 + \sum_j \left[ \frac{p_j^2}{2m_j} + \frac{1}{2} m_j \omega_j^2 (q_j - d_j)^2 \right] \quad (S3)$$

Here  $m_j$ ,  $p_j$  and  $q_j$  are respectively the mass, the momentum and the spatial coordinate of a particular vibrational mode,  $j$ , of frequency  $\omega_j$ . The excited electronic state is raised by the fundamental transition energy,  $\hbar\omega_{eg}^0$ , and is coupled linearly to the system coordinates via the displacement,  $d_j$ . The harmonic potentials,  $V(q)$ , are displayed in figure S2.

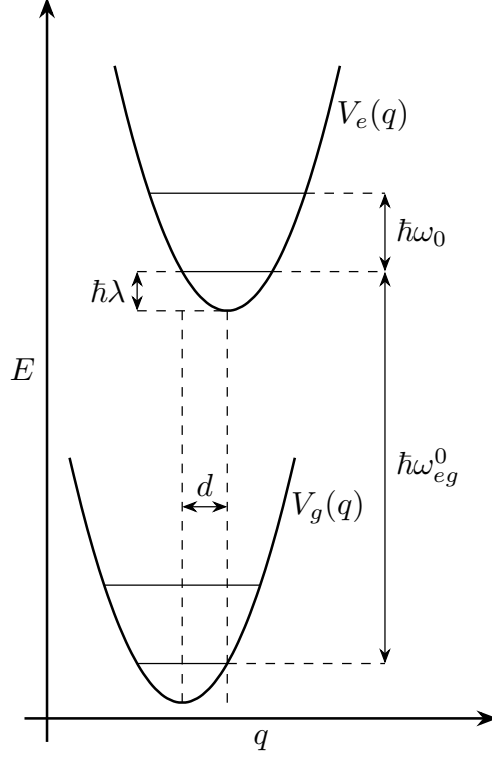


Figure S2: Potential Energy Surface of the displaced harmonic oscillator.

On conversion to a dimensionless coordinate system using,

$$P_j = \left(\sqrt{\hbar\omega_j m_j}\right)^{-1} p_j; \quad Q_j = \left(\sqrt{\frac{\omega_j m_j}{\hbar}}\right) q_j; \quad \Delta_j = \left(\sqrt{\frac{\omega_j m_j}{\hbar}}\right) d_j$$

the nuclear Hamiltonians can be written as,

$$h_g = \frac{1}{2} \sum_j \hbar\omega_j (P_j^2 + Q_j^2) = \sum_j \hbar\omega_j \left(b_j^\dagger b_j + \frac{1}{2}\right) \quad (\text{S4})$$

$$\begin{aligned} h_e &= \hbar\omega_{eg}^0 + \frac{1}{2} \sum_j \hbar\omega_j (P_j^2 + (Q_j - \Delta_j)^2) \\ &= \hbar\omega_{eg}^0 + \sum_j \hbar\omega_j \left(b_j^\dagger b_j - \frac{\Delta_j}{\sqrt{2}}(b_j + b_j^\dagger) + \frac{1}{2}\Delta_j^2 + \frac{1}{2}\right) \\ &= \hbar(\omega_{eg}^0 + \lambda) + \sum_j \hbar\omega_j \left(b_j^\dagger b_j - \frac{\Delta_j}{\sqrt{2}}(b_j + b_j^\dagger) + \frac{1}{2}\right) \end{aligned} \quad (\text{S5})$$

where  $P$  is the momentum,  $Q$  is the coordinate,  $\Delta$  is the excited state displacement and  $b^{(\dagger)}$

are the vibrational annihilation (creation) operators,

$$b^\dagger = \sqrt{\frac{m\omega}{2\hbar}} \left( q - \frac{i}{m\omega} p \right) = \frac{1}{\sqrt{2}} (Q - iP) \quad (\text{S6})$$

$$b = \sqrt{\frac{m\omega}{2\hbar}} \left( q + \frac{i}{m\omega} p \right) = \frac{1}{\sqrt{2}} (Q + iP) \quad (\text{S7})$$

such that,

$$b^\dagger b = \frac{1}{2} (Q - iP)(Q + iP)$$

$$Q = \frac{b + b^\dagger}{\sqrt{2}} \text{ and } P = \frac{b - b^\dagger}{i\sqrt{2}}$$

The reorganisation energy,  $\hbar\lambda$ , is related to the Huang-Rhys parameter,  $S$ , by

$$\lambda = \sum_j \lambda_j = \sum_j S_j \omega_j = \sum_j \frac{m_j \omega_j^2 d_j^2}{2\hbar} \quad (\text{S8})$$

$$S_j = \frac{1}{2} \Delta_j^2 = \frac{m_j \omega_j d_j^2}{2\hbar} \quad (\text{S9})$$

The system Hamiltonian is then diagonalised to incorporate the off-diagonal coupling terms and determine the accurate vibronic eigenfunctions. All simulations are completed using the adiabatic vibronic basis.

## Bath Hamiltonian

The environment is defined as an infinite ensemble of harmonic oscillators, such that the total bath Hamiltonian is given by,

$$H_B = \sum_n \sum_\alpha \left[ \frac{p_{n\alpha}^2}{2m_{n\alpha}} + \frac{1}{2} m_{n\alpha} \omega_{n\alpha}^2 x_{n\alpha}^2 \right] = \sum_n \sum_\alpha \hbar \omega_{n\alpha} \left( a_{n\alpha}^\dagger a_{n\alpha} + \frac{1}{2} \right) \quad (\text{S10})$$

Here,  $m_{n\alpha}$ ,  $p_{n\alpha}$  and  $\omega_{n\alpha}$  are respectively the mass, the momentum and the frequency of the mode,  $\alpha$ , of a particular bath,  $n$ . The bath mode coordinates are denoted  $x_{n\alpha}$  and  $a_{n\alpha}^{(\dagger)}$  are the lowering (raising) operators.

The bath modes couple linearly to the system, such that the total interaction Hamiltonian (including  $H_B$ ) is,

$$H_I = \sum_n \sum_\alpha \left[ \frac{p_{n\alpha}^2}{2m_{n\alpha}} + \frac{1}{2}m_{n\alpha}\omega_{n\alpha}^2 \left( x_{n\alpha} - \frac{g_{n\alpha}}{m_{n\alpha}\omega_{n\alpha}^2} B_n(q) \right)^2 \right] \quad (\text{S11})$$

where  $g_{n\alpha}$  is the dimensionless coupling strength and  $B_n(q)$  is a system operator which controls the action of the bath onto the system coordinates,  $q$ .<sup>7,8</sup>

The distribution of coupling strengths is described by the spectral density of each bath,  $J_n(\omega)$ .

$$J_n(\omega) = \sum_\alpha \frac{g_{n\alpha}^2}{2m_{n\alpha}\omega_{n\alpha}} \delta(\omega - \omega_{n\alpha}) \quad (\text{S12})$$

Every spectral density is assumed to have the Debye form for an overdamped Brownian oscillator,

$$J_n(\omega) = 2\eta_n \frac{\omega\gamma_n}{\omega^2 + \gamma_n^2} \quad (\text{S13})$$

In our model, we separate the environment into three baths to individually account for dephasing processes ( $n = 1$ ), intramolecular vibrational relaxation (IVR) ( $n = 2$ ) and fluorescence ( $n = 3$ ). The bath coupling operators are defined as,

$$B_1 = (-|g\rangle\langle g| + |e\rangle\langle e|) \otimes \sum_\nu |\nu\rangle\langle\nu| \quad (\text{S14})$$

$$B_2 = |g\rangle\langle b + b^\dagger| + |e\rangle\langle b + b^\dagger| \quad (\text{S15})$$

$$B_3 = \hat{\mu} = (|g\rangle\langle e| + |e\rangle\langle g|) \otimes \sum_\nu |\nu\rangle\langle\nu| \quad (\text{S16})$$

where  $\sum_\nu |\nu\rangle\langle\nu|$  is the identity operator over the nuclear degrees of freedom and  $\hat{\mu}$  is the dipole moment operator of the system. These operators are then transformed to the adiabatic vibronic basis using the same unitary transformation with which the system Hamiltonian was diagonalised.

As described in the main text, the spectral density parameters for the IVR and dephasing

phonon baths are set to be the same, whilst the coupling strength of the fluorescence bath is chosen to be very weak ( $\eta_3 = 1 \text{ cm}^{-1}$ ). This allows the definition of a complete model, whilst acknowledging that the fluorescence timescale of the porphyrin monomer is significantly slower (ca. 1 ns) than the timescale of the photon echo simulations ( $\leq 1 \text{ ps}$ ) in this study.

## Hierarchical Equations of Motion (HEOM)

For a bath of harmonic oscillators, the correlation function is related to the spectral density via,

$$C_n(t) = \frac{1}{\pi} \int_0^\infty d\omega J_n(\omega) \left( \coth\left(\frac{\beta\hbar\omega}{2}\right) \cos \omega t - i \sin \omega t \right) \quad (\text{S17})$$

where  $\beta$  is the inverse temperature, assumed the same for all baths.

The solution of this integral can be expressed as the sum of exponential terms,<sup>9</sup>

$$C_n(t) = \eta_n \gamma_n \left[ \left( \cot\left(\frac{\hbar\beta\gamma_n}{2}\right) - i \right) \exp(-\gamma_n t) + \sum_{k=1}^{\infty} \frac{8\pi k}{(2\pi k)^2 - (\hbar\beta\gamma_n)^2} \exp\left(-\frac{2\pi k t}{\hbar\beta}\right) \right] \quad (\text{S18})$$

which can then be re-expressed in terms of the bosonic Matsubara frequencies,  $\nu_{nk}; k = 0, 1, 2, \dots, M$ , and corresponding exponential prefactors,  $c_{nk}$ ,<sup>6,10</sup>

$$\begin{aligned} C_n(t) &= \eta_n \gamma_n \left[ \left( \cot\left(\frac{\hbar\beta\gamma_n}{2}\right) - i \right) \exp(-\nu_{n0} t) + \sum_{k=1}^M \frac{4\nu_{nk}}{\hbar\beta(\nu_{nk}^2 - \gamma_n^2)} \exp(-\nu_{nk} t) \right] \\ &= \sum_{k=0}^M c_{nk} e^{-\nu_{nk}|t|} \end{aligned} \quad (\text{S19})$$

$$\nu_{n0} = \gamma_n \quad (\text{S20})$$

$$\nu_{nk} = \frac{2\pi k}{\hbar\beta} \quad (\text{S21})$$

$$c_{n0} = \eta_n \gamma_n \left( \cot\left(\frac{\hbar\beta\gamma_n}{2}\right) - i \right) \quad (\text{S22})$$

$$c_{nk} = \frac{4\eta_n \gamma_n}{\hbar\beta} \left( \frac{\nu_{nk}}{\nu_{nk}^2 - \gamma_n^2} \right) \quad (\text{S23})$$

The evolution of the density matrix is separated into a hierarchy of auxiliary density operators (ADOs),  $\rho_{\mathbf{j}}$ , given by

$$\begin{aligned}
\dot{\rho}_{\mathbf{j}}(t) = & - \left( \frac{i}{\hbar} \mathcal{L} + \sum_{n=1}^N \sum_{k=0}^M \mathbf{j}_{nk} \nu_{nk} \right) \rho_{\mathbf{j}}(t) - i \sum_{n=1}^N \sum_{k=0}^M B_n^\times \rho_{\mathbf{j}_{nk}^+}(t) \\
& - i \sum_{n=1}^N \sum_{k=0}^M \mathbf{j}_{nk} \left( c_{nk} B_n \rho_{\mathbf{j}_{nk}^-}(t) - c_{nk}^* \rho_{\mathbf{j}_{nk}^-}(t) B_n \right) \\
& - \sum_{n=1}^N \left( \frac{2\eta_n}{\hbar\beta\gamma_n} - \eta_n \cot \left( \frac{\hbar\beta\gamma_n}{2} \right) - \sum_{k=1}^M \frac{c_{nk}}{\nu_{nk}} \right) B_n^\times B_n^\times \rho_{\mathbf{j}}(t) \quad (\text{S24})
\end{aligned}$$

where  $\mathcal{L}$  is the Liouvillian operator and  $B_n^\times \rho = [B_n, \rho]$  denotes the commutator of the bath coupling operator,  $B_n$ , and the density matrix.<sup>11</sup>

The ADOs are defined in terms of the  $N(M+1)$ -dimensional vectors  $\mathbf{j} = (j_{10}, \dots, j_{nk}, \dots, j_{NM})$  and  $\mathbf{j}^\pm = (j_{10}, \dots, j_{nk} \pm 1, \dots, j_{NM})$ , which contain elements for each Matsubara frequency of each bath. The coefficients of the vectors,  $j_{nk}$ , define the depth of the hierarchy for a particular ADO, with the true reduced density matrix equivalent to the ADO with all coefficients equal to zero.

The hierarchy must therefore be terminated with respect to the number of Matsubara frequencies involved and the depth associated with each frequency. We adopt the termination criterion of Dijkstra and Prokhorenko, who select a convergence parameter,  $\Gamma$ , beyond which the evolution is assumed to be within the Markovian limit.<sup>11</sup> The convergence parameter determines the number of Matsubara frequencies via,

$$\frac{2(M+1)\pi}{\beta} > \Gamma \quad (\text{S25})$$

and the hierarchy depth according to,

$$\sum_{n=1}^N \sum_{k=0}^M \mathbf{j}_{nk} \nu_{nk} > \Gamma \quad (\text{S26})$$

Here we choose  $\Gamma = 10\gamma_1$ , so that the convergence parameter is significantly faster than

the timescale of the bath fluctuations.

## Linear Absorption Spectrum

The linear absorption spectrum is calculated as the Fourier transform of the first order molecular response function,  $R^{(1)}(t_1)$ .<sup>9,12</sup>

$$\sigma_A(\omega) \propto \int_{-\infty}^{\infty} dt e^{i\omega t} R^{(1)}(t_1) \propto \int_{-\infty}^{\infty} dt e^{i\omega t} \text{Tr}_g \left( \hat{\mu} \hat{G}(t_1, t_0) [\hat{\mu}, \rho(-\infty)] \right) \quad (\text{S27})$$

Here the trace is taken over the ground state degrees of freedom only and the dynamical map  $\hat{G}(t_1, t_0)$  indicates use of the HEOM to propagate the result of the commutator from time  $t_0$  to time  $t_1$ .

## 2D Photon Echo Spectroscopy

The pulse sequence for four-wave mixing 2D photon echo spectroscopy is depicted in figure S3. Whilst  $\tau$ ,  $T$  and  $t$  define the separation of the pulse centres and the signal, as described in the main text, the interaction events can occur at any time under the Gaussian envelopes. Hence the separation of the interaction events is given by  $t_1$ ,  $t_2$  and  $t_3$ , which are the time references used in the double-sided Feynman diagrams presented below.<sup>13</sup>

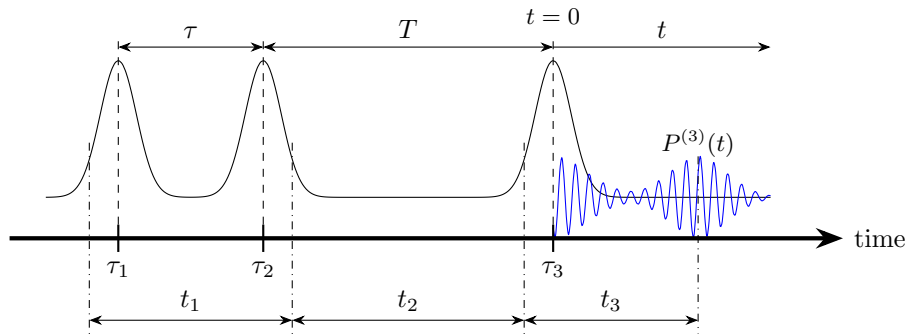


Figure S3: Pulse sequence for 2D Photon Echo Spectroscopy.

For a particular ordering of pulses, the rephasing wavevector is defined as,

$$\mathbf{k}_s = -\mathbf{k}_1 + \mathbf{k}_2 + \mathbf{k}_3 \quad (\text{S28})$$

with the non-rephasing wavevector as,

$$\mathbf{k}_s = \mathbf{k}_1 - \mathbf{k}_2 + \mathbf{k}_3 \quad (\text{S29})$$

By swapping the order in which the first two pulses arrive at the sample, the non-rephasing signal can be produced in the rephasing direction, equivalent to the use of negative coherence times ( $\tau < 0$ ).

Several non-linear fields are emitted from the sample in a photon echo measurement, but, importantly, the rephasing and non-rephasing signals involve a single interaction of the sample with each electric field.

## Equation of Motion-Phase Matching Approach (EOM-PMA)

The system-field interaction Hamiltonian is given by the semi-classical dipole approximation such that,

$$\begin{aligned} \hat{H}_{SF}(t) &= -\hat{\boldsymbol{\mu}} \cdot \mathcal{E}(\mathbf{r}, t) \\ &= -\sum_{m=1}^3 \hat{\boldsymbol{\mu}} \cdot (\chi_m E_m(t - \tau_m) \exp(-i\omega_m t + i\mathbf{k}_m \mathbf{r})) + c.c. \\ &= -\sum_{m=1}^3 \exp(i\mathbf{k}_m \mathbf{r}) \cdot V_m(t) + c.c. \end{aligned} \quad (\text{S30})$$

The total electric field,  $\mathcal{E}(\mathbf{r}, t)$ , is separated into three pulses with frequency  $\omega_m = 2\pi\nu_m$  and wavevector  $\mathbf{k}_m$ . The electric field strength is given by  $\chi_m$  and the field envelope,  $E_m(t - \tau_m)$ , centred at  $\tau_m$ , is assumed to be Gaussian,

$$E_m(t - \tau_m) = \exp\left(\frac{-(t - \tau_m)^2}{2\sigma^2}\right) = \exp\left(\frac{-4 \ln 2 (t - \tau_m)^2}{\tau_p^2}\right) \quad (\text{S31})$$

The full width at half maxima (FWHM) of the laser pulses in the time and frequency domains are,<sup>14,15</sup>

$$\text{time FWHM} = \tau_p = 2\sqrt{2 \ln 2} \sigma \quad (\text{S32})$$

$$\text{frequency FWHM} = \frac{4 \ln 2}{\pi c \tau_p} \quad (\text{S33})$$

Here, the spatial and temporal oscillations of the electric field have been separated to define the coupling operators,  $V_m(t)$ ,  $m = 1, 2, 3$ .

$$V_m(t) = (\hat{\mu} \chi_m E_m(t - \tau_m) \exp(-i\omega_m t)) \quad (\text{S34})$$

The system-field interaction Hamiltonian is incorporated into the Liouvillian operator as a time-dependent correction term,

$$\mathcal{L}\rho(t) = [H_S - H_{SF}(t), \rho(t)] = [H_S - \hat{\mu} \cdot \mathcal{E}(\mathbf{r}, t), \rho(t)] \quad (\text{S35})$$

The Liouvillian is then solved as part of the HEOM and propagated using equation S24.

In the knowledge that the rephasing and non-rephasing signals are produced in the phase matched direction,  $\mathbf{k}_s$ , after a single interaction with each of the three laser pulses, the Liouvillian can be re-expressed in terms of the coupling operators  $V_m(t)$  according to,

$$\mathcal{L}_1 \rho_1(t) = [H_S - H_{SF}(t), \rho_1(t)] = [H_S - V_1(t) - V_2^\dagger(t) - V_3^\dagger(t), \rho_1(t)] \quad (\text{S36})$$

The solution of this Liouvillian produces the non-Hermitian auxiliary  $\rho_1(t)$ , which accounts for a number of Liouville pathways, including the rephasing and non-rephasing contributions, as well as a multitude of other non-linear signals.

As described by Gelin et al, on considering the dependence of the non-Hermitian auxiliary

with respect to each laser field,  $\rho_1(\lambda_1, \lambda_2, \lambda_3; t)$  becomes a generating function for Liouville pathways which can be expanded as the Taylor series,<sup>16,17</sup>

$$\rho_1(\lambda_1, \lambda_2, \lambda_3; t) = \sum_{i,j,k=0}^{\infty} \lambda_1^i \lambda_2^j \lambda_3^k \rho_1^{i,j,k}(t) \quad (\text{S37})$$

The rephasing and non-rephasing Liouville pathways are associated with the  $\rho_1^{111}(t)$  contribution. This can be isolated by combining a series of permutations, where each of the field interactions are sequentially removed, according to equation S38.<sup>16</sup>

$$\begin{aligned} \lambda_1 \lambda_2 \lambda_3 \rho_1^{111}(t) &= \rho_1(\lambda_1, \lambda_2, \lambda_3; t) + \rho_1(\lambda_1, 0, 0; t) - \rho_1(\lambda_1, 0, \lambda_3; t) - \rho_1(\lambda_1, \lambda_2, 0; t) \\ &\quad - \rho_1(0, \lambda_2, \lambda_3; t) - \rho_1(0, 0, 0; t) + \rho_1(0, 0, \lambda_3; t) + \rho_1(0, \lambda_2, 0; t) \\ &\quad + O(\lambda_1^i \lambda_2^j \lambda_3^k), \quad i + j + k > 3 \end{aligned} \quad (\text{S38})$$

These permutations define eight auxiliary operators which each correspond to a unique Liouvillian. The auxiliary operators are defined as,

$$\begin{aligned} \rho_1 &= \rho_1(\lambda_1, \lambda_2, \lambda_3; t) \\ \rho_2 &= \rho_1(\lambda_1, \lambda_2, 0; t) \\ \rho_3 &= \rho_1(\lambda_1, 0, \lambda_3; t) \\ \rho_4 &= \rho_1(\lambda_1, 0, 0; t) \\ \rho_5 &= \rho_1(0, \lambda_2, \lambda_3; t) \\ \rho_6 &= \rho_1(0, \lambda_2, 0; t) \\ \rho_7 &= \rho_1(0, 0, \lambda_3; t) \\ \rho_8 &= \rho_1(0, 0, 0; t) \end{aligned}$$

producing seven relevant Liouvillians, as  $\rho_8$  defaults to the Liouville von-Neumann form.<sup>16,18</sup>

$$\mathcal{L}_1\rho_1(t) = -\frac{i}{\hbar} \left[ H_S - V_1(t) - V_2^\dagger(t) - V_3^\dagger(t), \rho_1(t) \right] \quad (\text{S39})$$

$$\mathcal{L}_2\rho_2(t) = -\frac{i}{\hbar} \left[ H_S - V_1(t) - V_2^\dagger(t), \rho_2(t) \right] \quad (\text{S40})$$

$$\mathcal{L}_3\rho_3(t) = -\frac{i}{\hbar} \left[ H_S - V_1(t) - V_3^\dagger(t), \rho_3(t) \right] \quad (\text{S41})$$

$$\mathcal{L}_4\rho_4(t) = -\frac{i}{\hbar} [H_S - V_1(t), \rho_4(t)] \quad (\text{S42})$$

$$\mathcal{L}_5\rho_5(t) = -\frac{i}{\hbar} \left[ H_S - V_2^\dagger(t) - V_3^\dagger(t), \rho_5(t) \right] \quad (\text{S43})$$

$$\mathcal{L}_6\rho_6(t) = -\frac{i}{\hbar} \left[ H_S - V_2^\dagger(t), \rho_6(t) \right] \quad (\text{S44})$$

$$\mathcal{L}_7\rho_7(t) = -\frac{i}{\hbar} \left[ H_S - V_3^\dagger(t), \rho_7(t) \right] \quad (\text{S45})$$

The macroscopic polarization in the phase-matched direction is then calculated using,

$$P_{\mathbf{k}_s}^{(3)}(\tau, T, t) = \exp(i\mathbf{k}_s\mathbf{r})\mathbf{Tr}(\hat{\mu}(\rho_1(t) - \rho_2(t) - \rho_3(t) + \rho_4(t) - \rho_5(t) + \rho_6(t) + \rho_7(t))) + c.c. \quad (\text{S46})$$

where the isolation of the rephasing/non-rephasing phase-matched contribution from equation S38 has been reproduced by the combination of the evolved auxiliary states. The number of Liouvillians required can be reduced by enforcing the rotating wave approximation, but here we adopt the full form to keep the model general.<sup>17,18</sup>

The third order polarization is calculated as the expectation value of the dipole moment operator and the combined states, where the spatial oscillations have been factorised out into the exponential prefactor, following the initial definition of the system-field interaction Hamiltonian, equation S30.

The spatial component is calculated according to the pulse sequence in figure S3, using

$$\mathbf{k}_1 \cdot \mathbf{r} = \omega(\tau_1) \quad (\text{S47})$$

$$\mathbf{k}_2 \cdot \mathbf{r} = \omega(\tau_1 + \tau) \quad (\text{S48})$$

$$\mathbf{k}_3 \cdot \mathbf{r} = \omega(\tau_1 + \tau + T) \quad (\text{S49})$$

where  $\tau_1$  is the time from the beginning of the simulation to the centre of the first laser pulse.

The exponential prefactor for the rephasing signal is therefore given by,

$$\exp(i\mathbf{k}_s \mathbf{r}) = \exp(i(-\mathbf{k}_1 + \mathbf{k}_2 + \mathbf{k}_3) \mathbf{r}) = \exp(i\omega(\tau_1 + 2\tau + T)) \quad (\text{S50})$$

with the non-rephasing prefactor by,

$$\exp(i\mathbf{k}_s \mathbf{r}) = \exp(i(\mathbf{k}_1 - \mathbf{k}_2 + \mathbf{k}_3) \mathbf{r}) = \exp(i\omega(\tau_1 + T)) \quad (\text{S51})$$

2D photon echo spectra are then calculated as the double Fourier transform of the third order polarization with respect to  $\tau$  and  $t$ .<sup>15,19</sup> The rephasing spectra require an inverse transformation with respect to the coherence time ( $\propto \exp[-i\omega_\tau \tau]$ ), whilst the non-rephasing require a forwards transformation ( $\propto \exp[+i\omega_\tau \tau]$ ).

$$S_{\text{PE}}(\omega_\tau, T, \omega_t) = \int_{-\infty}^{\infty} dt \int_{-\infty}^{\infty} d\tau \exp[\mp i\omega_\tau \tau] \exp[+i\omega_t t] iP_{\mathbf{k}_s}^{(3)}(\tau, T, t) \quad (\text{S52})$$

## Initial Conditions

We assume factorised initial conditions, where the system and bath are completely uncorrelated prior to the simulation, and the system density matrix is initially defined as a Boltzmann distribution over the vibrational levels of the ground electronic state.

# Liouville pathway analysis

For the specific case of the displaced harmonic oscillator with two electronic states, each coupled to two vibrational levels, there are 32 double-sided Feynman diagrams that survive the rotating wave approximation. Here we limit the analysis to pathways which have a starting population in the lowest vibrational level of the ground electronic state,  $|g_0\rangle$ , and the pathways are assigned following the 2D electronic spectroscopy convention of  $R_{1-4}$ .

Non-oscillatory population pathways are removed from the data via fit of a single exponential function to the oscillations along the population time. Performing a Fourier transform of the residuals then produces amplitude spectra which distinguish positively and negatively oscillating coherence pathways. Here we identify positive coherences,  $\propto e^{+i\omega_0 T}$ , in blue and negative coherences,  $\propto e^{-i\omega_0 T}$ , in red such that,

$$|g_0\rangle \langle g_1| \propto e^{+i\omega_0 T}; \quad |g_1\rangle \langle g_0| \propto e^{-i\omega_0 T}$$

The population and coherence pathways for ground state bleach and stimulated emission processes are labelled using colour-coded symbols, as defined in table S1.

**Table S1: Symbol Key for Liouville pathways.**

	Ground State Bleach	Stimulated Emission
Population	▲	■
Positive Coherence ( $+\omega_0$ )	△	□
Negative Coherence ( $-\omega_0$ )	△	□

All 32 Liouville pathways are presented in figures S4 - S7 as double-sided Feynman diagrams (see SI of reference 1). These diagrams are drawn in the usual manner, with the transition frequencies associated with each interaction written out explicitly alongside.

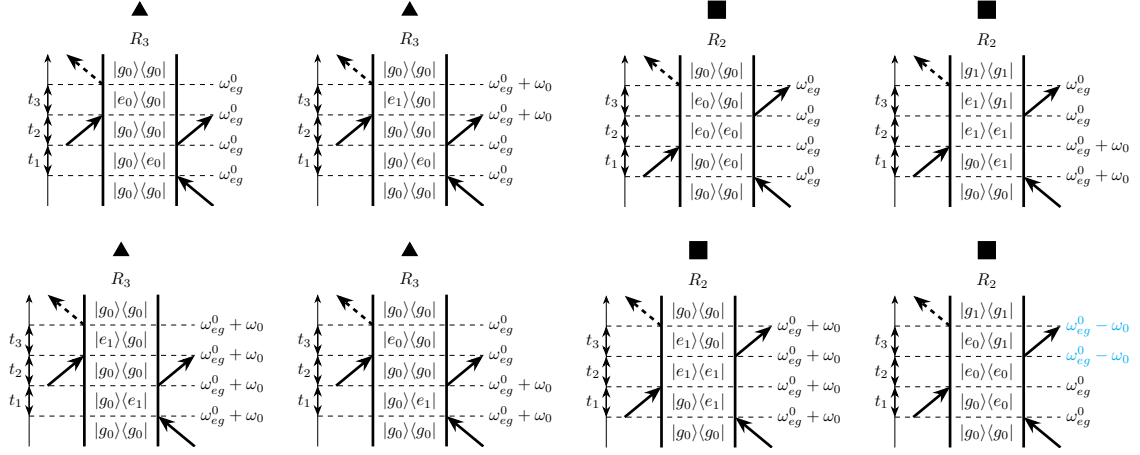


Figure S4: Rephasing Population Pathways.

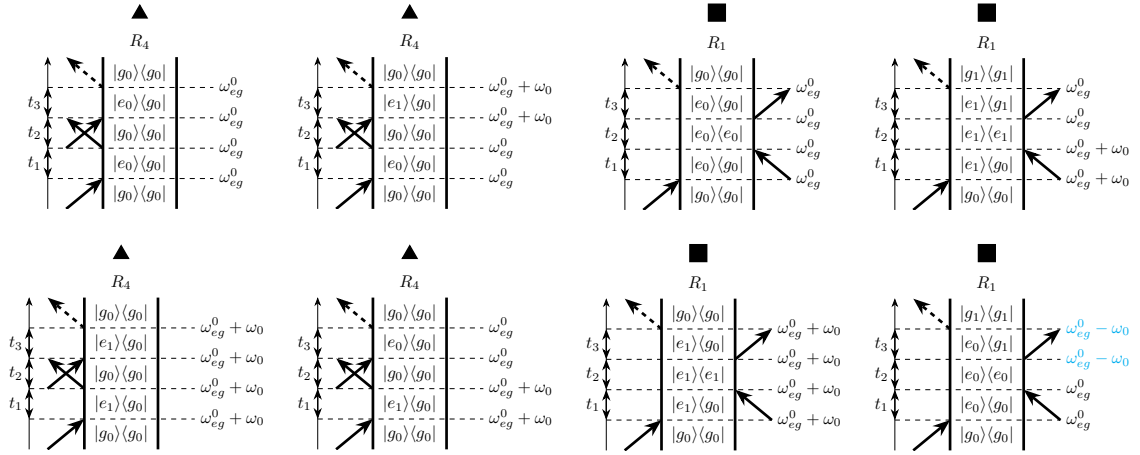


Figure S5: Non-Rephasing Population Pathways.

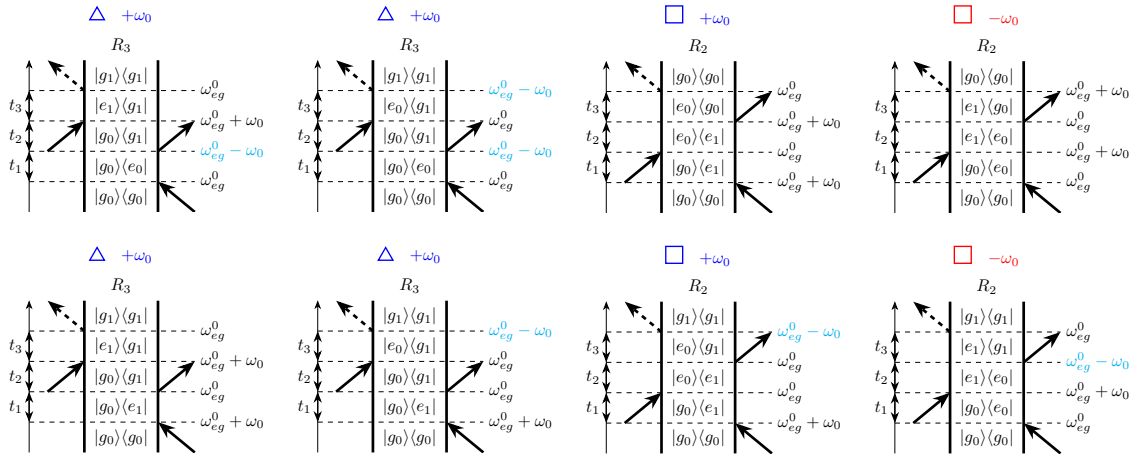


Figure S6: Rephasing Coherence Pathways.

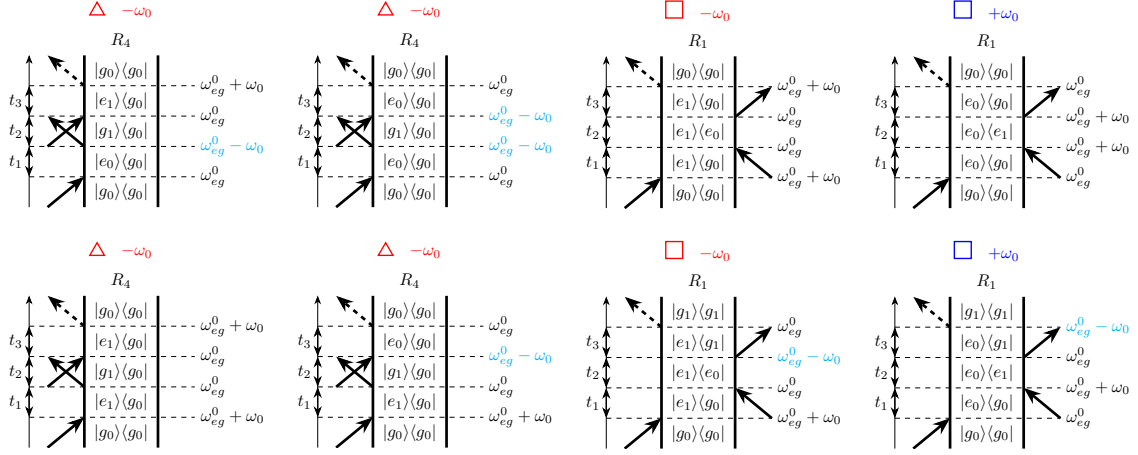


Figure S7: Non-Rephasing Coherence Pathways.

For the centred laser spectrum simulation, all 32 pathways contribute, with the peak locations predicted as shown in figure S8 for the rephasing and non-rephasing spectra. Here the population pathways have been included, identifying peak locations to which they would contribute, were they not removed from the amplitude spectra by the exponential fitting procedure, as described above.

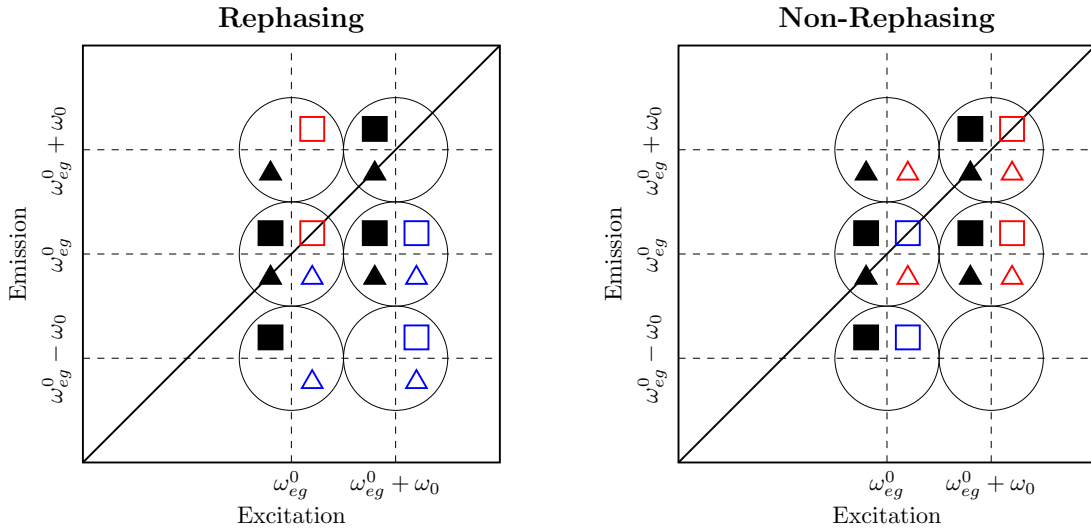


Figure S8: Peak location key diagram for the centred laser spectrum simulation, including population pathways, for Rephasing (left) and Non-Rephasing (right) amplitude spectra. The Liouville pathways are assigned as per table S1, producing peaks in the spectra identified by the encompassing black circles.

On blue-shifting the laser spectrum, all pathways involving the  $\omega_{eg}^0 - \omega_0$  transition frequency (highlighted cyan in figures S4 - S7) are eliminated from the spectra. This results in the loss of the lower emission frequency peaks from the amplitude spectra, as shown in figure S9.

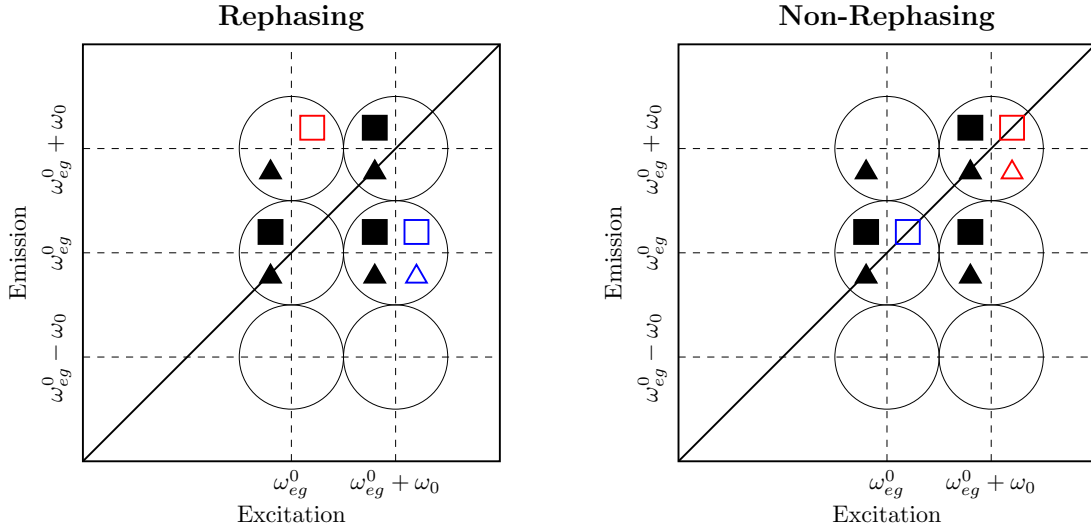


Figure S9: Peak location key diagram for the blue-shifted laser spectrum simulation, including population pathways, for Rephasing (left) and Non-Rephasing (right) amplitude spectra. The Liouville pathways are identified as per table S1, producing peaks in the spectra identified by the encompassing black circles.

## Additional 2D Spectra Examples

Summaries of calculated rephasing and non-rephasing 2D spectra (real, normalised) for both the centred and blue-shifted laser spectrum simulations are provided below.

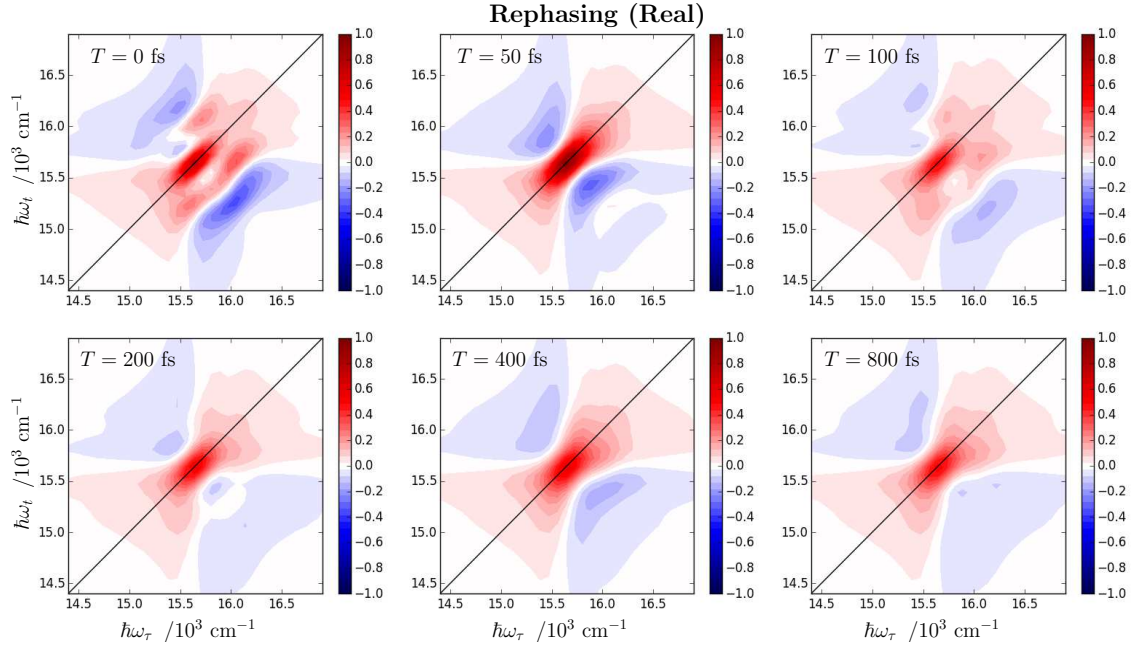


Figure S10: Rephasing (real) spectra for the centred laser spectrum simulation.

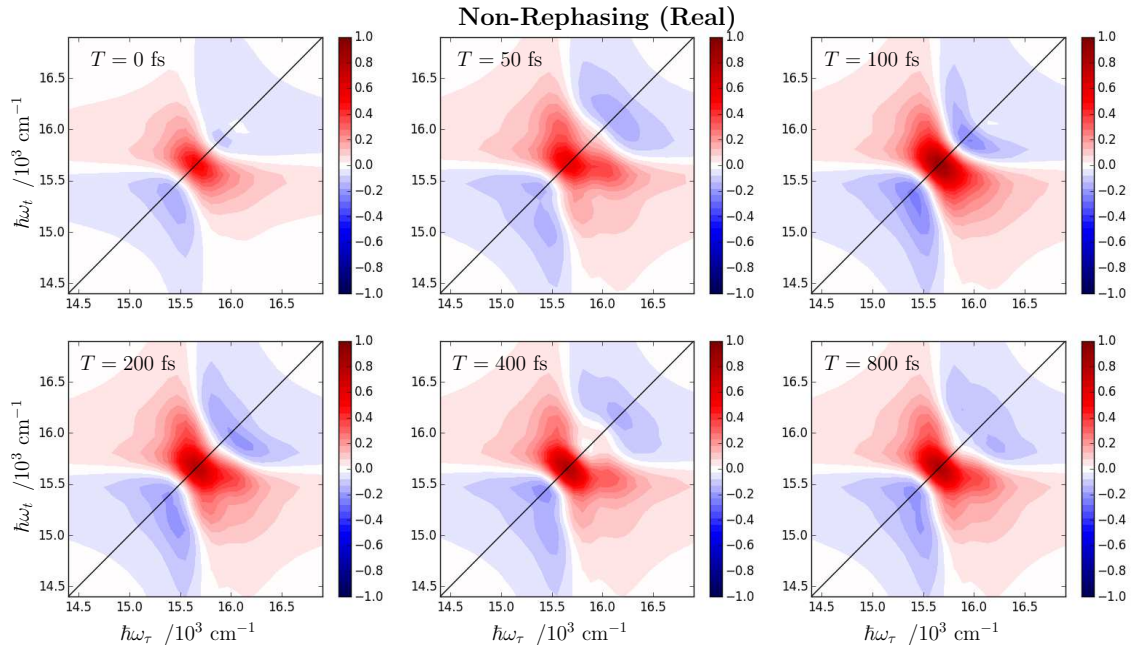


Figure S11: Non-Rephasing (real) spectra for the centred laser spectrum simulation.

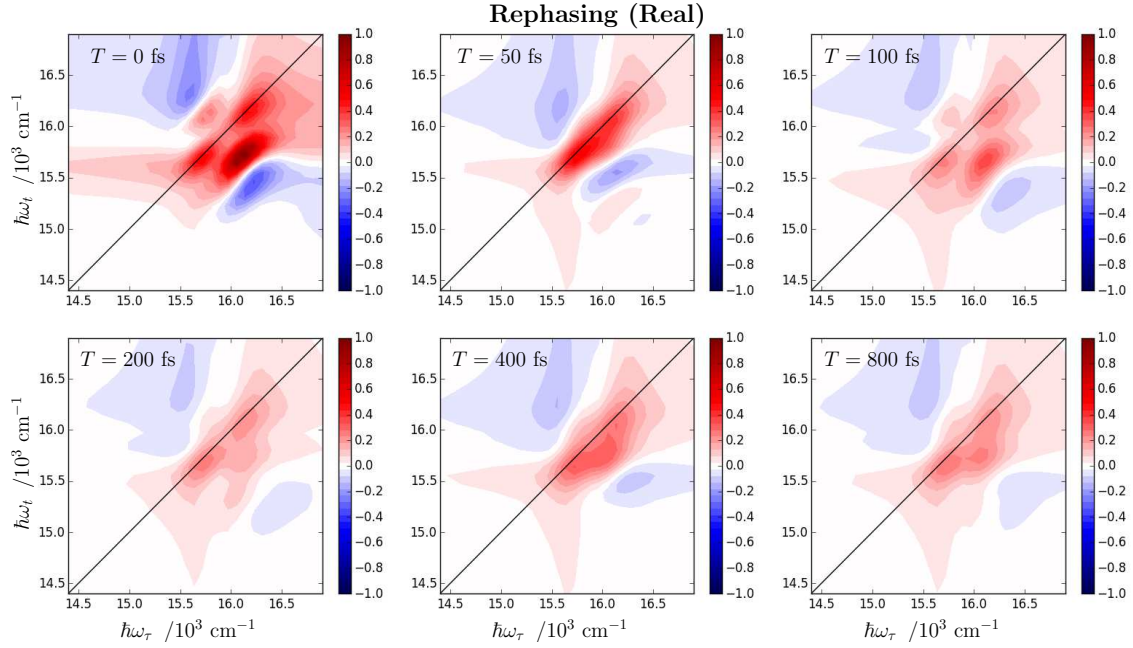


Figure S12: Rephasing (real) spectra for the blue-shifted laser spectrum simulation.

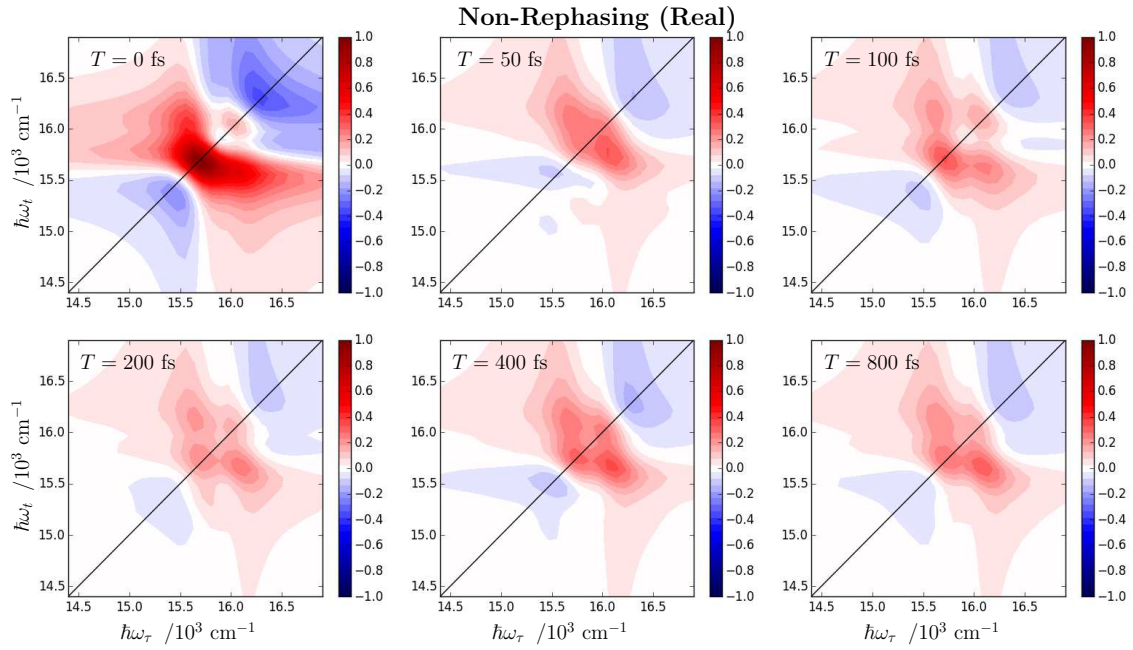


Figure S13: Non-Rephasing (real) spectra for the blue-shifted laser spectrum simulation.

## Computational Details

The evolution of the auxiliary density operators is solved using the fourth order Runge-Kutta method and FORTRAN 90, with a time step of 0.05 fs. Construction of the system and all other manipulations were performed using Python, making use of the standard NumPy and matplotlib packages, as well as the quantum object class of the QuTiP (Quantum Toolbox in Python) package.<sup>20,21</sup>

## References

- (1) Camargo, F. V. A.; Grimmelsmann, L.; Anderson, H. L.; Meech, S. R.; Heisler, I. A. Resolving Vibrational from Electronic Coherences in Two-Dimensional Electronic Spectroscopy: The Role of the Laser Spectrum. *Phys. Rev. Lett.* **2017**, *118*, 033001.
- (2) Camargo, F. V. A.; Anderson, H. L.; Meech, S. R.; Heisler, I. A. Full Characterization of Vibrational Coherence in a Porphyrin Chromophore by Two-Dimensional Electronic Spectroscopy. *J. Phys. Chem. A* **2015**, *119*, 95–101.
- (3) Drobizhev, M.; Stepanenko, Y.; Dzenis, Y.; Karotki, A.; Rebane, A.; Taylor, P. N.; Anderson, H. L. Extremely Strong Near-IR Two-Photon Absorption in Conjugated Porphyrin Dimers: Quantitative Description with Three-Essential-States Model. *J. Phys. Chem. B* **2005**, *109*, 7223–7236.
- (4) Camargo, F. V. A. Unravelling Vibrational and Electronic Coherences via Two-Dimensional Electronic Spectroscopy of Zinc-Porphyrins. Ph.D. thesis, University of East Anglia, 2017.
- (5) Kim, S. Y.; Joo, T. Coherent Nuclear Wave Packets in Q States by Ultrafast Internal Conversions in Free Base Tetraphenylporphyrin. *J. Phys. Chem. Lett.* **2015**, *6*, 2993–2998.

- (6) Mukamel, S. *Principles of Nonlinear Optical Spectroscopy*; Oxford University Press: New York, 1995.
- (7) Dijkstra, A. G.; Tanimura, Y. Linear and Third- and Fifth-Order Nonlinear Spectroscopies of a Charge Transfer System Coupled to an Underdamped Vibration. *J. Chem. Phys.* **2015**, *142*, 212423.
- (8) Tanimura, Y. Stochastic Liouville, Langevin, Fokker-Planck, and Master Equation Approaches to Quantum Dissipative Systems. *J. Phys. Soc. Jpn.* **2006**, *75*, 082001.
- (9) Chen, L.; Zheng, R.; Shi, Q.; Yan, Y. Optical Line Shapes of Molecular Aggregates: Hierarchical Equations of Motion Method. *J. Chem. Phys.* **2009**, *131*, 094502.
- (10) Dijkstra, A. G.; Tanimura, Y. System Bath Correlations and the Nonlinear Response of Qubits. *J. Phys. Soc. Jpn.* **2012**, *81*, 063301.
- (11) Dijkstra, A. G.; Prokhorenko, V. I. Simulation of Photo-Excited Adenine in Water with a Hierarchy of Equations of Motion Approach. *J. Chem. Phys.* **2017**, *147*, 064102.
- (12) Tanimura, Y. Reduced Hierarchy Equations of Motion Approach with Drude plus Brownian Spectral Distribution: Probing Electron Transfer Processes by means of Two-Dimensional Correlation Spectroscopy. *J. Chem. Phys.* **2012**, *137*, 22A550.
- (13) Brixner, T.; Mančal, T.; Stiopkin, I. V.; Fleming, G. R. Phase-Stabilized Two-Dimensional Electronic Spectroscopy. *J. Chem. Phys.* **2004**, *121*, 4221–4236.
- (14) Sharp, L. Z.; Egorova, D.; Domcke, W. Efficient and Accurate Simulations of Two-Dimensional Electronic Photon-Echo Signals: Illustration for a Simple Model of the Fenna-Matthews-Olson Complex. *J. Chem. Phys.* **2010**, *132*, 014501.
- (15) Leng, X.; Yue, S.; Weng, Y.-X.; Song, K.; Shi, Q. Effects of Finite Laser Pulse Width on Two-Dimensional Electronic Spectroscopy. *Chem. Phys. Lett.* **2017**, *667*, 79–86.

- (16) Gelin, M. F.; Egorova, D.; Domcke, W. Efficient Method for the Calculation of Time- and Frequency-Resolved Four-Wave Mixing Signals and its Application to Photon-Echo Spectroscopy. *J. Chem. Phys.* **2005**, *123*, 164112.
- (17) Gelin, M. F.; Egorova, D.; Domcke, W. Efficient Calculation of Time- and Frequency-Resolved Four-Wave-Mixing Signals. *Acc. Chem. Res.* **2009**, *42*, 1290–1298.
- (18) Cheng, Y.-C.; Lee, H.; Fleming, G. R. Efficient Simulation of Three-Pulse Photon-Echo Signals with Application to the Determination of Electronic Coupling in a Bacterial Photosynthetic Reaction Center . *J. Phys. Chem. A* **2007**, *111*, 9499–9508.
- (19) Cheng, Y.-C.; Engel, G. S.; Fleming, G. R. Elucidation of Population and Coherence Dynamics using Cross-Peaks in Two-Dimensional Electronic Spectroscopy. *Chem. Phys.* **2007**, *341*, 285–295.
- (20) Johansson, J.; Nation, P.; Nori, F. QuTiP: An Open-Source Python Framework for the Dynamics of Open Quantum Systems. *Comput. Phys. Commun.* **2012**, *183*, 1760–1772.
- (21) Johansson, J.; Nation, P.; Nori, F. QuTiP 2: A Python Framework for the Dynamics of Open Quantum Systems. *Comput. Phys. Commun.* **2013**, *184*, 1234–1240.